

PAPER

## Inter-crystal scattering event identification using a novel silicon photomultiplier signal multiplexing method

To cite this article: Hyeong Seok Shim *et al* 2023 *Phys. Med. Biol.* **68** 115008

View the [article online](#) for updates and enhancements.

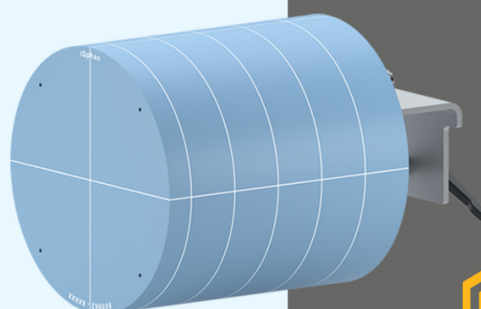
### You may also like

- [Design study of a PET detector with 0.5 mm crystal pitch for high-resolution preclinical imaging](#)  
Xi Zhang, Hongsen Yu, Qiangqiang Xie *et al.*
- [Time-over-threshold for pulse shape discrimination in a time-of-flight phoswich PET detector](#)  
Chen-Ming Chang, Joshua W Cates and Craig S Levin
- [Performance evaluation of a staggered three-layer DOI PET detector using a 1 mm LYSO pitch with PETsys TOFPET2 ASIC: comparison of HAMAMATSU and KETEK SiPMs](#)  
Tim Binder, Han Gyu Kang, Munetaka Nitta *et al.*

## Introducing IQphan™ Comprehensive Image Quality Phantom

IQphan is a single phantom that addresses QA across the range of different CT scanner specifications.

[Learn more >](#)



**See IQphan  
at RSNA:**  
Mirion Medical  
booth #6328

 **SUN NUCLEAR**



## PAPER

## Inter-crystal scattering event identification using a novel silicon photomultiplier signal multiplexing method

RECEIVED  
19 February 2023REVISED  
20 April 2023ACCEPTED FOR PUBLICATION  
28 April 2023PUBLISHED  
22 May 2023Hyeong Seok Shim<sup>1,2,3</sup>, Sangjin Bae<sup>1,2,3</sup>, Seungeun Lee<sup>3,4</sup> and Jae Sung Lee<sup>1,2,3,5</sup> <sup>1</sup> Interdisciplinary Program of Bioengineering, Seoul National University, Seoul, Republic of Korea<sup>2</sup> Integrated Major in Innovative Medical Science, Seoul National University Graduate School, Republic of Korea<sup>3</sup> Department of Nuclear Medicine, Seoul National University College of Medicine, Seoul, Republic of Korea<sup>4</sup> Department of Biomedical Sciences, Seoul National University College of Medicine, Seoul, Republic of Korea<sup>5</sup> Brightonix Imaging Inc., Seoul, Republic of KoreaE-mail: [jaes@snu.ac.kr](mailto:jaes@snu.ac.kr)

Keywords: PET, inter-crystal scattering, signal multiplexing, neural network, machine learning

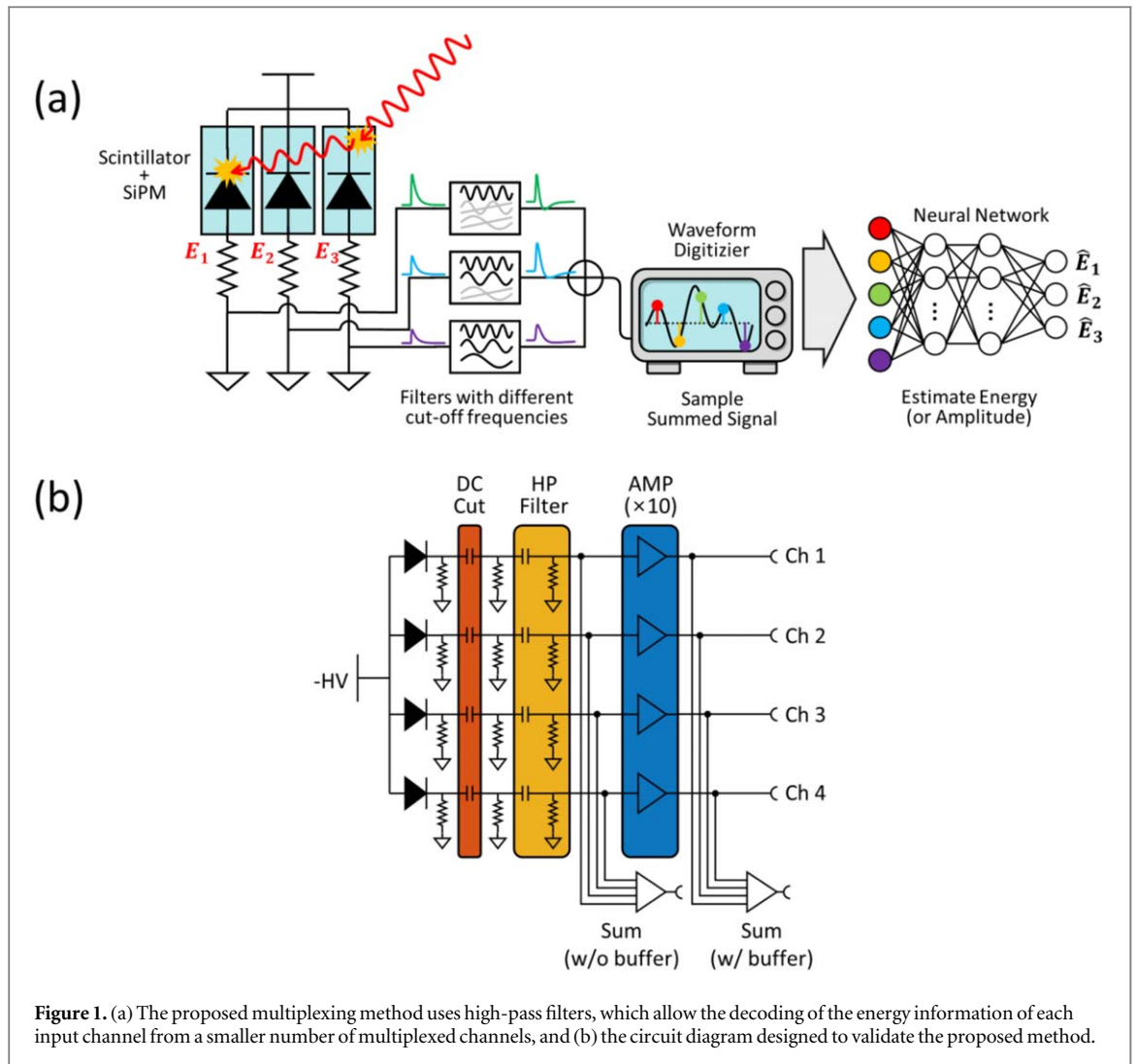
**Abstract**

*Objective.* Identifying the inter-crystal scatter (ICS) events and recovering the first interaction position enables the accurate determination of the line-of-response in positron emission tomography (PET). However, conventional silicon photomultiplier (SiPM) signal multiplexing methods based on two-dimensional (2D) charge-division circuits do not allow the detection of multiple gamma-ray interaction positions in a scintillation array coupled with a SiPM array. In this study, we propose a novel multiplexing method that can restore all the individual channel data from a smaller number of multiplexed channels using high-pass filters and neural networks. *Approach.* The number of output channels is reduced by summing the SiPM signals that have passed through high-pass filters with different time constants. Then, the signal amplitude of each SiPM channel is restored from the combined signal using an artificial neural network. This study explains the principle of this method in detail and demonstrates the results using 4:1 multiplexing as an example. The usefulness of this method was also demonstrated by its application in the identification of ICS events in 1-to-1 coupled LSO-SiPM PET detectors. *Main results.* The artificial neural network enabled accurate energy estimation for each SiPM channel. One of the high-pass filter sets with the lowest Cramér–Rao lower bound provided the best results, yielding  $R^2$  value of 0.99 between the true and estimated signals. The energy and flood histograms generated using the best-estimated signals were in good agreement with the ground truth. Additionally, the proposed method accurately estimated 2D energy deposit distribution in the LSO crystal array, allowing ICS event identification. *Significance.* The proposed method is potentially useful for ICS event recovery with a reduced number of array signal readout channels from a SiPM array.

**1. Introduction**

Positron emission tomography (PET) is a functional and molecular imaging technique that employs the detection of two 511 keV gamma-rays produced through the mutual annihilation of positrons emitted by a radiotracer. Radiation detectors used in PET systems consist of scintillation crystals and photosensors. The scintillation crystal converts high-energy gamma-rays into low-energy scintillation photons, and the photosensors detect low-energy photons and convert them into electrical signals. Silicon photomultiplier (SiPM) is a widely used photosensor in PET systems. The size of SiPMs ranges from  $1 \times 1$  to  $4 \times 4$  mm. The high granularity and reduced scintillation photon loss due to the compact size of the SiPM contributed to the improved spatial and energy resolution of the PET detectors.

However, the increased number of output channels in the photosensor array is a disadvantage caused by the compact size and high granularity of SiPM. Therefore, various signal multiplexing methods have been proposed to efficiently read and record signals from the SiPM arrays by reducing the number of output channels, while



preserving the time, energy, and position information for gamma-ray detection (Park *et al* 2022). Most multiplexing methods used in SiPM PET detectors are based on two-dimensional (2D) charge division circuits, such as Anger logic and discretized positioning circuits (Yamamoto *et al* 2011, Downie *et al* 2013, Goertzen *et al* 2013, Ko *et al* 2013, Olcott *et al* 2013, Won *et al* 2016, Park *et al* 2017). Usually, these methods obtain the  $x$  and  $y$  coordinates of the gamma-ray interaction based on the ratio of the two readouts in each direction. Therefore, only four readouts ( $x^+$ ,  $x^-$ ,  $y^+$ , and  $y^-$ ) are required to specify where the gamma-rays are absorbed, thereby substantially reducing the number of readout channels (e.g. 16:1, 36:1, or greater). Additionally, by utilizing charge-division-based signal multiplexing methods, we can achieve a higher intrinsic spatial resolution for PET detectors compared to that of the pitch of the SiPM element (e.g. Ko *et al* 2016).

On the other hand, these charge division-based signal multiplexing methods have a critical disadvantage that only a single gamma-ray interaction position can be estimated from the dataset obtained with a single event trigger. Therefore, using these methods, it is a challenge to distinguish inter-crystal scatter (ICS) events, where gamma-rays partially lose energy through Compton scatterings before being absorbed by photo-electric absorption in neighboring crystal, from pure photo-electric absorption or intra-crystal scatter events, where gamma-rays lose all their energy in a crystal element. The ICS events results in a degradation of the spatial resolution and image contrast of PET imaging system. Utilizing larger scintillation crystal elements reduces the ICS events, however, it may result in degradation of PET spatial resolution. Identifying ICS events and recovering the first interaction position allows for the accurate determination of the line-of-response (LOR), which is the straight line connecting two opposite gamma-ray interaction positions and providing information on the location of radiotracer in the body. There are several studies using time-over-threshold (ToT) method to achieve Compton scattering detection (Sharma *et al* 2020, Park and Lee 2020, Shimazoe *et al* 2020, Kim *et al* 2022, Uenomachi *et al* 2022). J-PET uses plastic scintillators which have low density and stopping power, resulting in a high level of scatter occurring within the scintillator. Therefore, it is important to measure the energy to determine whether a signal is a photoelectric or Compton scattering event (Sharma *et al* 2020). Because

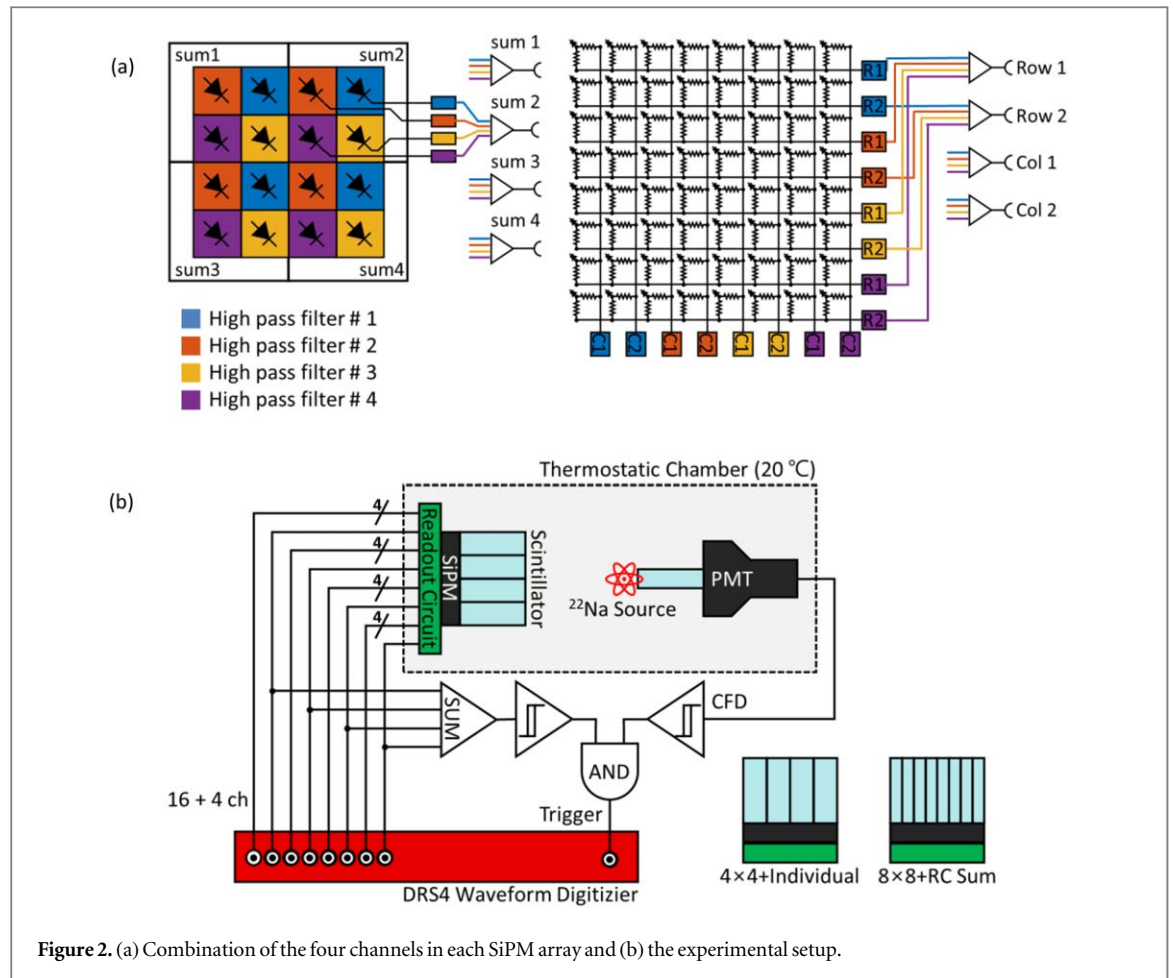


Figure 2. (a) Combination of the four channels in each SiPM array and (b) the experimental setup.

Compton imaging is based on events in which Compton scattering occurs, accurate estimation of the position and energy of Compton scattering is required (Shimazoe *et al* 2020, Kim *et al* 2022, Uenomachi *et al* 2022). Improved versions of ToT, such as dynamic ToT (Shimazoe *et al* 2020, Kim *et al* 2022) and PETNET (Uenomachi *et al* 2022), were used to determine the scattered energy more accurately. A multiplexing method using delay-chained ToT pulses has been proposed (Park *et al* 2020) for ICS event detection. However, the ToT requires as many comparators and/or FPGA I/O pins as the number of SiPM channels.

The row-and-column sum method (Popov *et al* 2006, Kwon and Lee, 2014, Stolin *et al* 2014) can identify ICS events because it can estimate the positions of two or more interactions from a dataset measured along the directions of row and column. However, the row-and-column sum method requires more readout channels than 2D charge division circuits ( $2N$  versus 4) for  $N \times N$  SiPM arrays.

Here, we propose a novel multiplexing method using high-pass filters that allows the decoding of the energy information of each input channel from a smaller number of multiplexed channels (figure 1). In the proposed method, the number of output channels is reduced by summing the SiPM signals that have passed through passive first-order high-pass filters with different time constants (or cutoff frequencies). To restore the energy information of each SiPM, we evaluated two decoding methods (pseudo-inverse and artificial neural networks). As a proof of concept, we demonstrated 4:1 multiplexing as an example. Additionally, we applied the proposed method to ICS event identification using a PET detector with  $4 \times 4$  and  $8 \times 8$  array-type SiPMs.

## 2. Materials and methods

### 2.1. Multiplexing method

The scintillation crystals and SiPM devices used in PET detectors have slightly different characteristics, and the delay and dispersion of the electrical signals differ depending on the SiPM position. Therefore, the detector response determined by the pulse shape difference is position-dependent. However, the position dependence of the detector response is not sufficiently large to estimate the gamma-ray interaction position using only the position-dependent detector response (shape of the signals readout by SiPM) and conventional pulse-shape analysis methods.

The main idea of the proposed method is to modify the detector response by applying an electrical filter to the SiPM signal such that the filtered signals can be distinguished from each other based on their pulse shape. The contributions to the summed (multiplexed) signal by each SiPM can be estimated if the filtered signal is uncorrelated or the correlation is sufficiently small. Here, the ‘contribution’ is proportional to the energy of gamma-rays deposited on the corresponding scintillation crystal.

In this study, to minimize circuit complexity and dead time, passive first-order high-pass filters with different resistor and capacitor values were applied. The detector response, determined by several factors, including sensor characteristics, high-pass filter, and circuit routing, was first measured by uniformly irradiating the detector block with a 511 keV source. The output signal of a multiplexer consisting of high-pass filters and summing amplifiers was then modeled as a linear combination of the normalized detector responses and deposited energy (more precisely, the weights applied to the normalized detector response), as shown in figure 1 and equation (1).

The demultiplexing process is equivalent to solving the inverse problem to estimate the deposited energy information from a digitally sampled multiplexer output, given a normalized detector response. Among the several approaches to solving the linear inverse problem, we chose the pseudo-inverse method and artificial neural networks because of their simplicity in designing and implementing the data collection chain.

## 2.2. Experimental setup

Figure 1(b) shows a circuit diagram designed to validate the proposed method. To investigate whether signal buffering was necessary, the high-pass filtered SiPM signals were summed either before or after buffering using summing amplifiers. The summed signal was digitized using a waveform sampler with a sufficiently high sampling rate and wide bandwidth so that no signal shape information was lost.

The three detector modules tested in this study employed a  $4 \times 4$  array-type SiPM (S14160-3050HS-04; HPK, Japan) or  $8 \times 8$  array-type SiPM (S14160-3050HS-08; HPK, Japan), which have the same SiPM element size and pitch (3.0 and 3.12 mm). The  $4 \times 4$  and  $8 \times 8$  SiPMs were 1-to-1 coupled with  $4 \times 4$  and  $8 \times 8$  LSO crystal arrays, respectively. The size of a crystal element was  $3.0 \times 3.0 \times 15 \text{ mm}^3$  and the pitch length between the crystal elements was 3.12 mm. Additionally, light-shared detectors were made using an  $8 \times 8$  SiPM coupled with a  $12 \times 12$  LSO crystal array (crystal element size =  $2.0 \times 2.0 \times 20 \text{ mm}^3$ ). The crystal elements were optically isolated using the ESR reflectors. Four different high-pass filters were applied to the signals from the four SiPM channels of the  $4 \times 4$  SiPM and each of the four row/column summed channels of the  $8 \times 8$  SiPM, as shown in figure 2(a). The filtered signals were combined using the summing amplifiers (AD8000; Analog Devices, US) before and after passing through the buffers. The summed signals and four ground truth signals (high-pass filtered signals before summation) were sampled using a 1 GHz digitizer (DT5742B; CAEN, Italy). The number of samples for each event was 1024, which yielded approximately 1  $\mu\text{s}$  long sampled signals.

Using the best set of high-pass filters determined by the methods described in section 2.4, four multiplexing circuits with high-pass filters, buffers, and a summing amplifier were applied to the  $4 \times 4$  and  $8 \times 8$  SiPMs. Therefore, a total of four summing signals and 16 ground-truth signals were measured, as shown in figure 2(b). For gamma-ray irradiation, a point source of 224.59 kBq (6.07  $\mu\text{Ci}$ )  $^{22}\text{Na}$  was used. Furthermore, for coincidence measurement, a reference detector consisting of a  $4 \times 4 \times 10 \text{ mm}^3$  LYSO crystal and a single-channel fast PMT (R9800; HPK, Japan) (Lee *et al* 2011) was used. All the experiments were performed at 20 °C inside a thermostatic chamber, and the over-voltage of SiPMs were set at 2.3 V in all the experiments.

## 2.3. Energy estimation algorithms

### 2.3.1. Mathematical modeling

The following assumptions were made to simplify the mathematical modeling and devise methods for estimating the energy deposited in each crystal by gamma-ray incidence.

1. The shape of the output pulse, hereafter referred to as the normalized detector response, was determined by several factors including the decay time of the scintillation crystal and the time constant of the filter, which does not vary according to the deposited energy. Additionally, the pulse amplitude was determined from the deposited energy.
2. The noise characteristics of front-end electronics follow a normal distribution (additive and white Gaussian) and are not affected by the shape or amplitude of the pulses.
3. The multiplexed electric signals are recorded using a waveform sampler.

Based on the assumptions above, any multiplexing circuit can be modeled as a linear system using the following equation (Lee *et al* 2018):

**Table 1.** Resistor ( $\Omega$ ) and capacitor (pF), and cut-off frequency (MHz) values for the tested high-pass filter sets.

Set	CRLB	Ch 1			Ch 2			Ch 3			Ch 4		
		$R$	$C$	$f_c$	$R$	$C$	$f_c$	$R$	$C$	$f_c$	$R$	$C$	$f_c$
1	Lowest	150	91	11.66	1200	91	1.457	5000	91	0.350	5000	1000	0.032
2	Lowest	200	91	8.745	1200	91	1.457	5000	91	0.350	5000	1000	0.032
3	Lowest	150	91	11.66	750	120	1.768	5000	91	0.350	5000	1000	0.032
4	Lowest	240	91	7.287	820	91	2.133	1600	220	0.452	5000	1000	0.032
5	Modest	100	91	17.49	620	1000	0.257	1200	1000	0.133	3000	1000	0.053
6	Modest	100	91	17.49	680	220	1.064	150	1000	1.061	750	680	0.312
7	Highest	270	120	4.912	200	560	1.421	270	560	1.053	820	220	0.882
8	Highest	1200	91	1.457	270	470	1.254	620	220	1.167	750	820	0.259

$$\mathbf{y} = \mathbf{A}\mathbf{x} + \mathbf{n}, \quad (1)$$

$\mathbf{x} \in \mathbb{R}^m$ ,  $x_i \geq 0 \forall i \in \{1 \dots m\}$ : individual energy transferred to each crystal from gamma-rays.  $m$  is the number of sensors (SiPMs coupled to the crystal).

$\mathbf{y} \in \mathbb{R}^s$ : multiplexed (summed) signal acquired using waveform sampler.  $s$  is the number of waveform samples (e.g. 1024).

$\mathbf{A} \in \mathbb{R}^{s \times m}$ : a matrix defined by the multiplexing circuit. Each column vector was determined using the normalized detector response.

$\mathbf{n} \in \mathbb{R}^s$ ,  $\mathbf{n} \sim N(0, \sigma^2 \mathbf{I}_s)$ : zero-mean additive white Gaussian noise (AWGN)

In this study, to obtain a noise-robust multiplexing technique, the matrix  $\mathbf{A}$  and the estimation algorithm were optimized. First, we chose a set of time constants for filters that yielded a low variance in the energy estimation, as described in section 2.4. Then, to solve the inverse problem determined by a set of filters, we applied two different individual deposit energy estimation methods: (1) pseudo-inverse and (2) artificial neural networks.

### 2.3.2. Pseudo inverse method

Because AWGN was assumed, the maximum-likelihood solution of equation (1) can be directly calculated using the pseudo-inverse of the detector response matrix  $\mathbf{A}$  as follows (Lee *et al* 2018):

$$\hat{\mathbf{x}} = (\mathbf{A}^T \mathbf{A})^{-1} \mathbf{A}^T \mathbf{y}. \quad (2)$$

### 2.3.3. Artificial neural network

We can easily estimate the energy using a pseudo-inverse matrix calculation; however, this method does not allow the imposition of constraints on the solution (e.g. non-negativity of  $\mathbf{x}$ ) to obtain an accurate answer. Although a convex-constrained optimization method was proposed to solve the demultiplexing problem, it requires iterative estimation of the solution  $\mathbf{x}$ . Moreover, it has not succeeded in demultiplexing the signals multiplexed by 2D charge division circuits (Lee *et al* 2018). Therefore, in this study, we developed an artificial neural network-based energy estimation method that provides a solution through a single feedforward operation once it is trained.

A multi-layer perceptron was trained to infer the energy of the filtered signals ( $O \times 1$ ,  $O$ : number of filtered signals = number of network output nodes) from the sampled multiplexed signal input ( $S \times 1$ ,  $S$ : number of samples = number of network input nodes). The network had two hidden layers, and the number of nodes in the hidden layer was 256. We used the ReLU activation function and did not employ normalization or dropout. In our experimental setup, the network input was a  $1024 \times 1$  vector of the summed signal, and the output was a  $4 \times 1$  vector of the filtered signal energy. Approximately 40 000 events per filter combination were used as datasets, which were split into training, validation, and test sets at a ratio of 5:1:4.

## 2.4. Optimization of high pass filters

To determine the best combination of high-pass filters, we measured the detector responses of 207 different high-pass filters, which were made by combining 23 resistors (0.1–5.1 k $\Omega$ ) and 9 capacitors (91–1000 pF).

To accurately restore the energy of each input signal from the summed signal, the characteristics of the input signals should differ as much as possible. The accuracy of the energy estimation increased as the variance of the estimators decreased. Therefore, we searched resistor and capacitor combinations that yield low Cramér–Rao lower bound (CRLB) of a given linear system. Under the assumptions in section 2.3.1, the CRLB of a given linear system can be derived as follows:

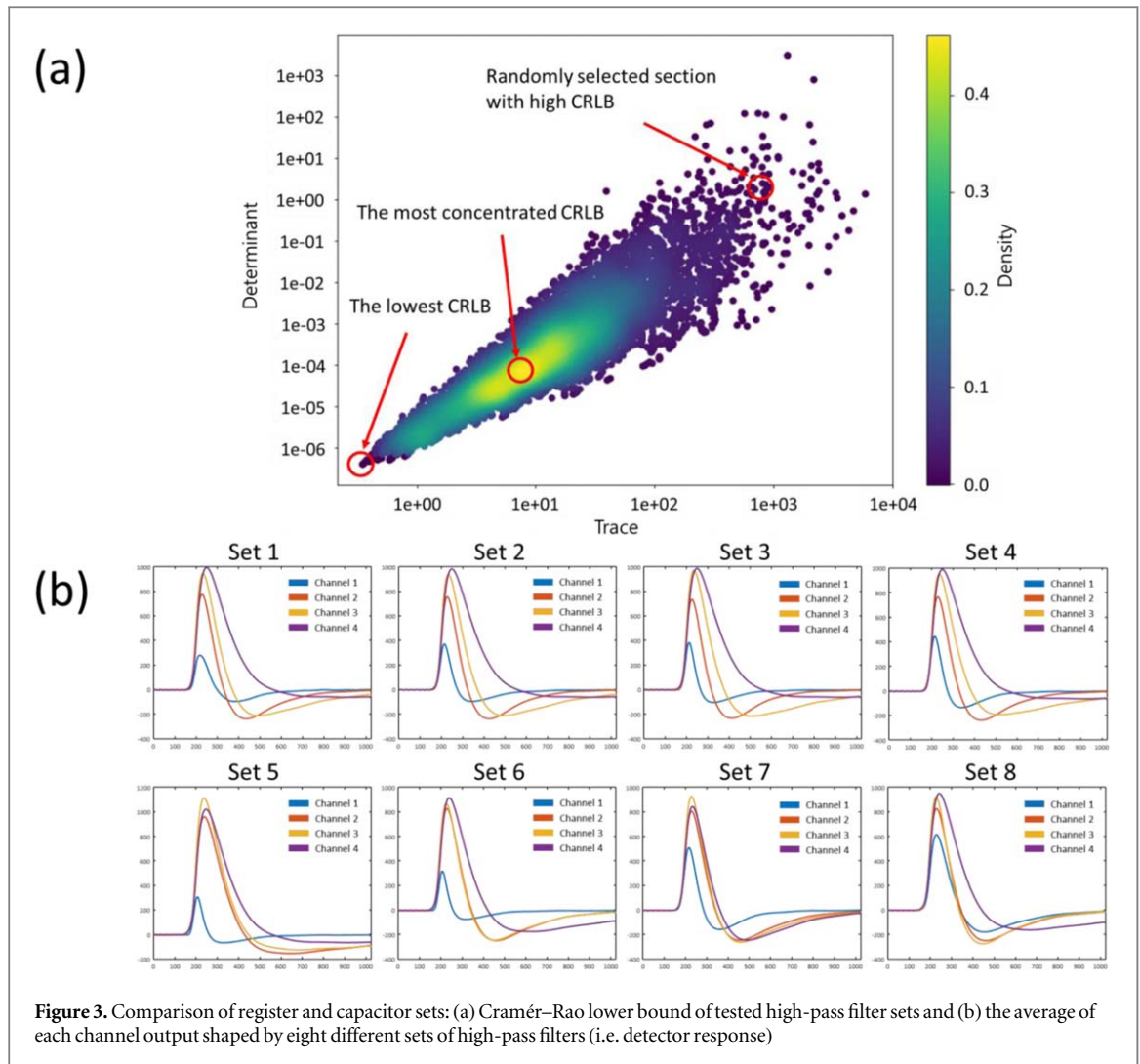


**Figure 3.** Comparison of register and capacitor sets: (a) Cramér–Rao lower bound of tested high-pass filter sets and (b) the average of each channel output shaped by eight different sets of high-pass filters (i.e. detector response)

$$\text{Var}(\hat{x}) \geq \text{CRLB}(\hat{x}) = \sigma^2(\mathbf{A}^T \mathbf{A})^{-1}. \quad (3)$$

Because we assumed the variance of AWGN to be independent of  $\mathbf{A}$ , we can ignore the  $\sigma^2$  term. In our case, the CRLB is a  $4 \times 4$  matrix; thus, instead of directly comparing the CRLB, we used the determinant (covariance of different signals) and trace (variance of each signal) of the CRLB as representative values to compare the filter combinations. Based on the CRLB of the estimated solution, we selected the resistor–capacitor combinations listed in table 1. Sets 1–4 had the lowest determinant and trace values, Sets 5 and 6 had moderate values, and Sets 7 and 8 had the highest values (figure 3(a)). Figure 3(b) shows the average output of each channel shaped by eight different sets of high-pass filters (i.e. the detector response). Sets 1–4 yielded well-differentiated pulse shapes, whereas Sets 5–8 resulted in the overlapping of at least two pulses.

To determine the best set of high-pass filters out of the eight candidate sets, we calculated the coefficient of determination ( $R^2$ ) of the linear regression between the estimated (by the neural network) and true energies. Additionally, the energy resolution of the photopeak in the energy spectrum was measured using the estimated energy.

## 2.5. Detector-level performance

We applied the best high-pass filter sets to each of four channels of the  $4 \times 4$  array-type SiPM and each of the four row/column summed channels of the  $8 \times 8$  array-type SiPM, multiplexing the 16 channels into four readouts. To verify the energy estimation performance, in addition to the four multiplexed channels, the signal of each input channel was received separately as the ground truth. For each channel, the coefficient of determination between the estimated and true energies was calculated. For the  $4 \times 4$  array SiPM, energy resolution was measured at each channel. When an energy higher than 100 keV was measured in two or more channels, it was considered that ICS has occurred. Additionally, the ratio of the photoelectric to ICS events was measured.

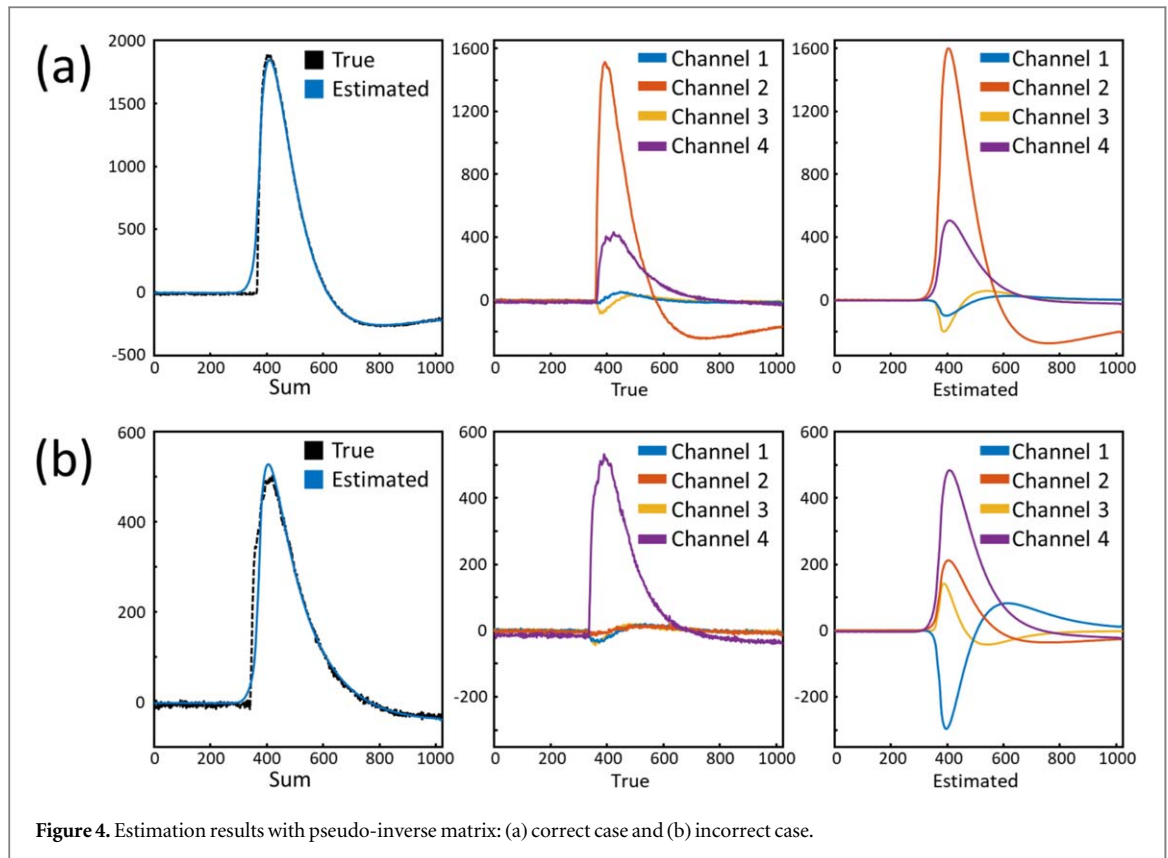


Figure 4. Estimation results with pseudo-inverse matrix: (a) correct case and (b) incorrect case.

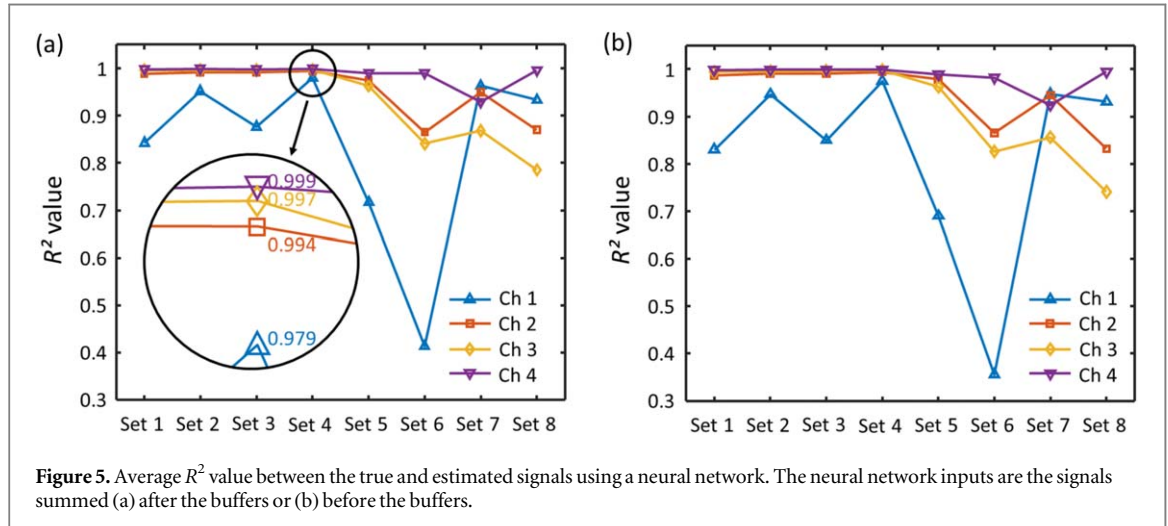
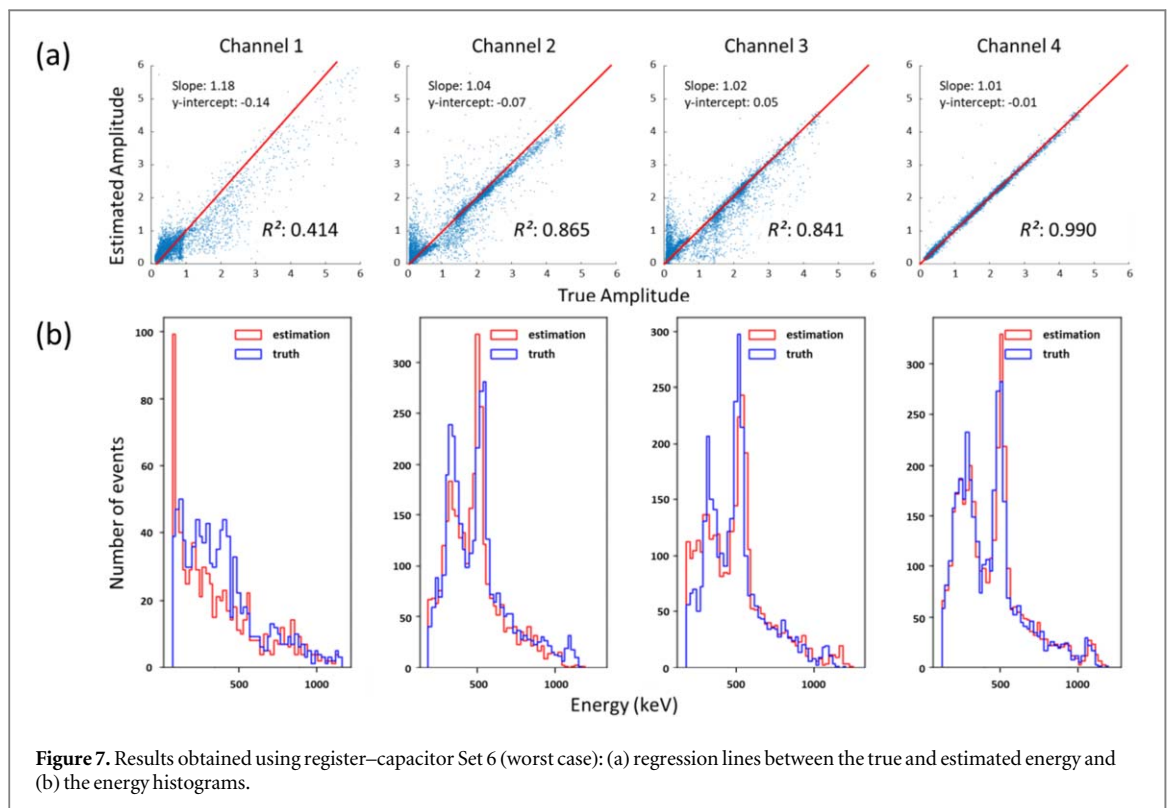
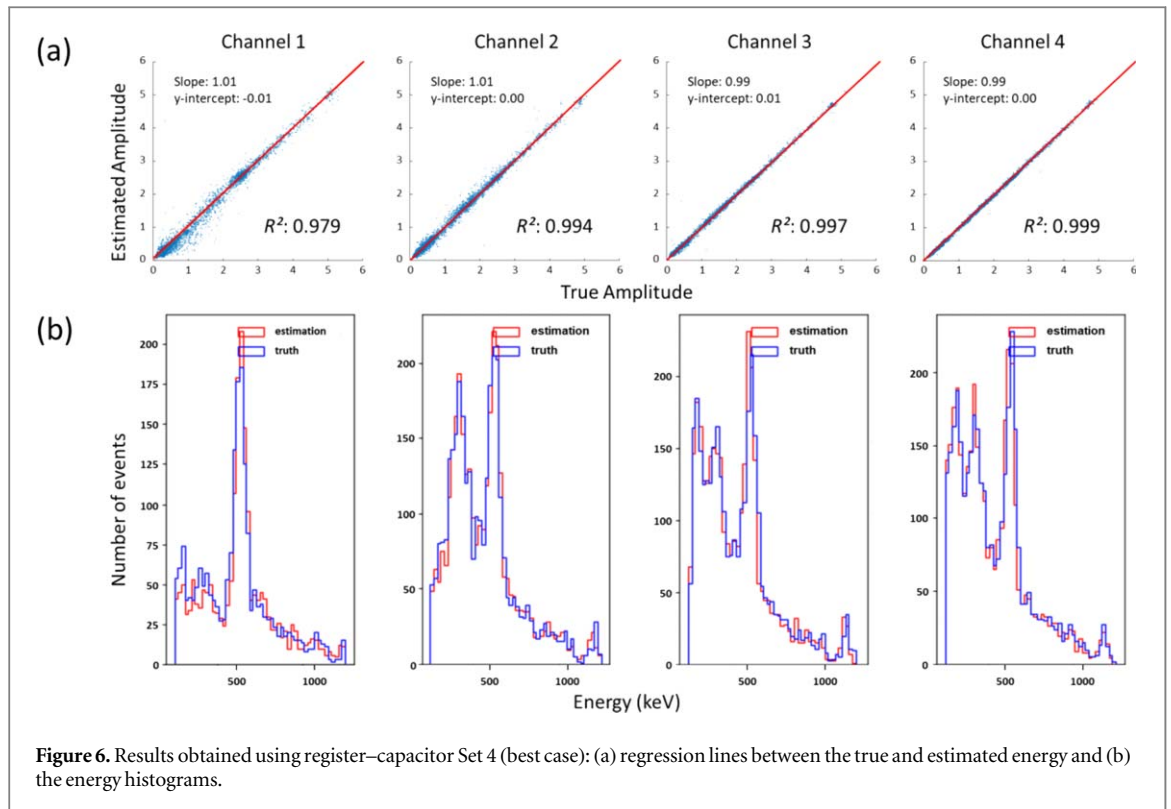


Figure 5. Average  $R^2$  value between the true and estimated signals using a neural network. The neural network inputs are the signals summed (a) after the buffers or (b) before the buffers.

### 3. Results

#### 3.1. Pseudo inverse method

Figure 4 shows two representative cases: (a) correct estimation results and (b) incorrect estimation results, which were obtained by applying the pseudo-inverse method. The first column in figure 4 shows the measured (summed or multiplexed, black line) and estimated ( $A \cdot x$ , blue lines) signals that are in good agreement with each other. The second and third columns show the actual high-pass-filtered signals before the summation and their estimates (i.e. each column vector of  $A \times x_i$ , normalized detector response  $\times$  energy estimate), respectively. As shown in this figure, pseudo-inverse matrices often fail to estimate the energy and recover the input signal, resulting in physically infeasible negative energy values. Therefore, no further analysis was performed on the results of the pseudo-inverse method.



### 3.2. Optimization of high pass filters

Figure 5(a) shows the estimation results with the signal summed after the buffers (the average  $R^2$  between the true and restored signals). Sets 1–4, which had the lowest CRLB, performed better than Sets 5–8, which had modest or high CRLB values. Among Sets 1–4, Set 4 exhibited the best results, with the highest average  $R^2$  values. Figure 5(b) shows the estimation results with the signal summed before the buffers. Both the results show the same tendency, indicating that the effect of the buffer on the performance of the proposed method is negligible.

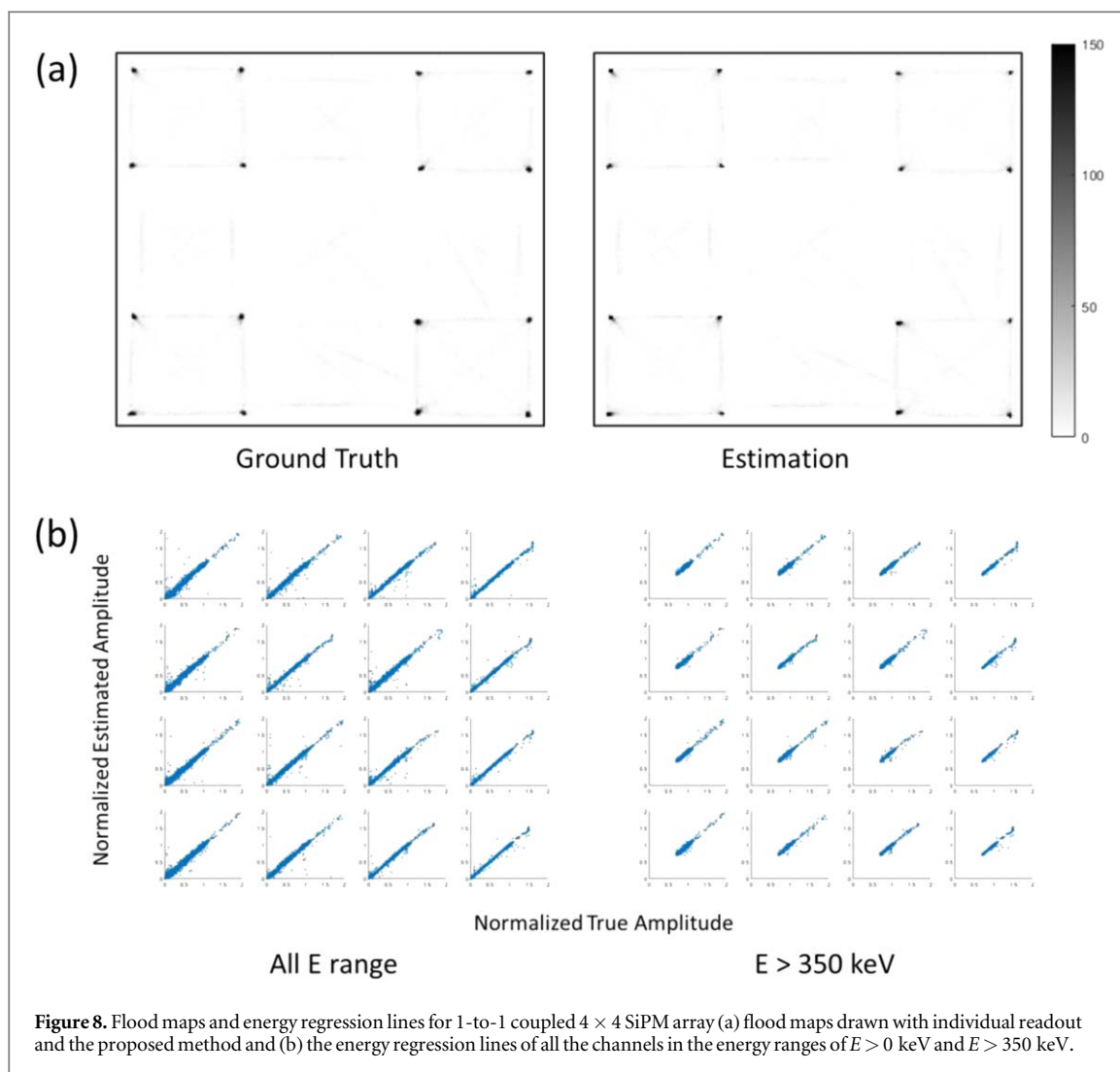


Figure 8. Flood maps and energy regression lines for 1-to-1 coupled  $4 \times 4$  SiPM array (a) flood maps drawn with individual readout and the proposed method and (b) the energy regression lines of all the channels in the energy ranges of  $E > 0$  keV and  $E > 350$  keV.

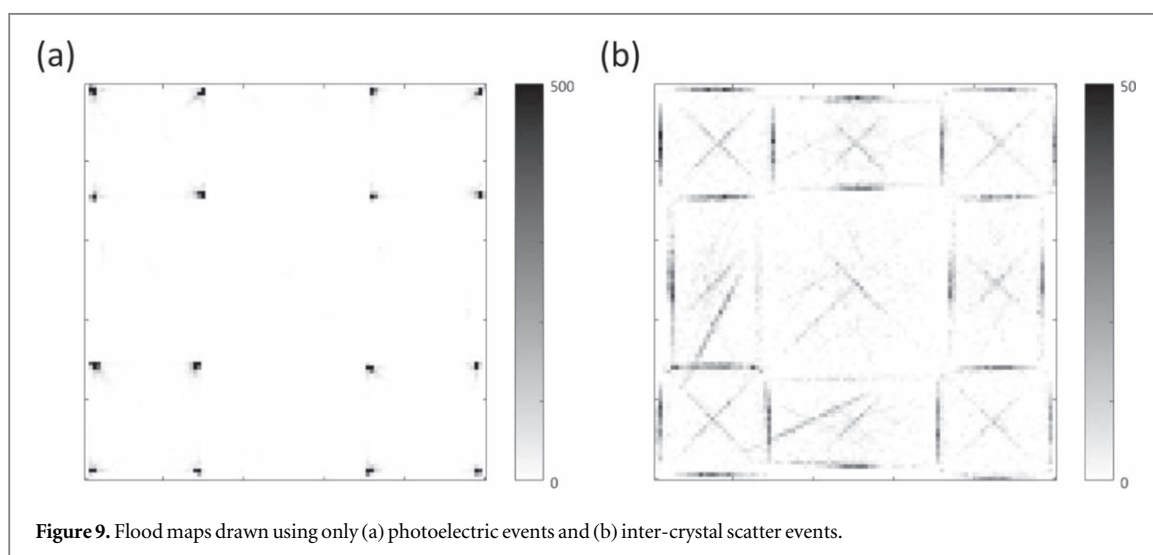
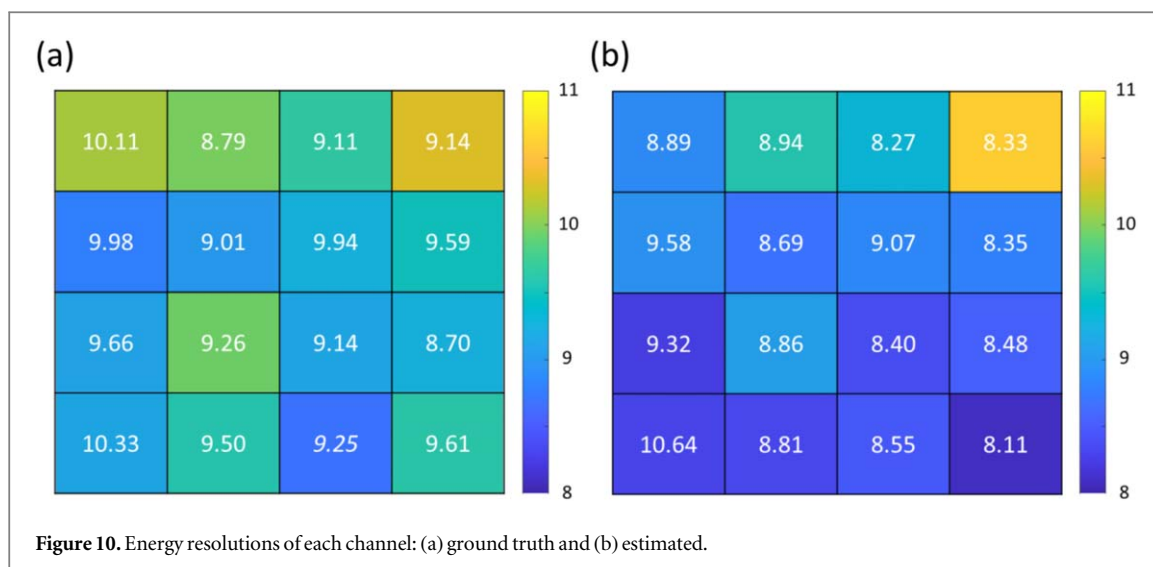


Figure 9. Flood maps drawn using only (a) photoelectric events and (b) inter-crystal scatter events.

Set 4 showed the largest  $R^2$  values (0.979, 0.994, 0.997, and 0.999 for each of the four channels, respectively) when estimating the energy of the signal using the neural network from the summed signals generated before passing through the buffers (figure 6(a)). The  $R^2$  value depends on the time constant of the filter. The smaller the energy is, the less accurate is the estimation. All four trend lines between the estimated energy and the ground truth had the slope between  $1.00 \pm 0.01$  and the  $y$ -intercept between  $0.00 \pm 0.01$ . The peak of the energy histogram drawn based on the estimated energy agreed well with the true histogram (figure 6(b)). The energy



resolutions of each of the four channels with the estimated energy were 10.2%, 12.6%, 11.7%, and 11.2%, and those with the ground truth were 11.4%, 12.4%, 12.8%, and 11.9% respectively. Figure 7 shows the results of Set 6, which exhibited the lowest  $R^2$  values. 80 000 events were collected when plotting regression lines.

### 3.3. Detector-level performance: $4 \times 4$ SiPM

Figure 8(a) shows the flood maps generated using the center-of-gravity algorithm (Park and Lee, 2020) applied to the true and estimated energies of the  $4 \times 4$  SiPM output signals. To verify the estimation accuracy, the ground truth and estimated value of the energy in each channel were compared. Figure 8(b) shows the scatter plots of the true and estimated energies of the  $4 \times 4$  SiPM output signals. Considering the full energy range, the average  $R^2$  values for all the channels were above 0.99. Considering the signals above 350 keV, the lowest  $R^2$  value among the 16 channels was 0.944.

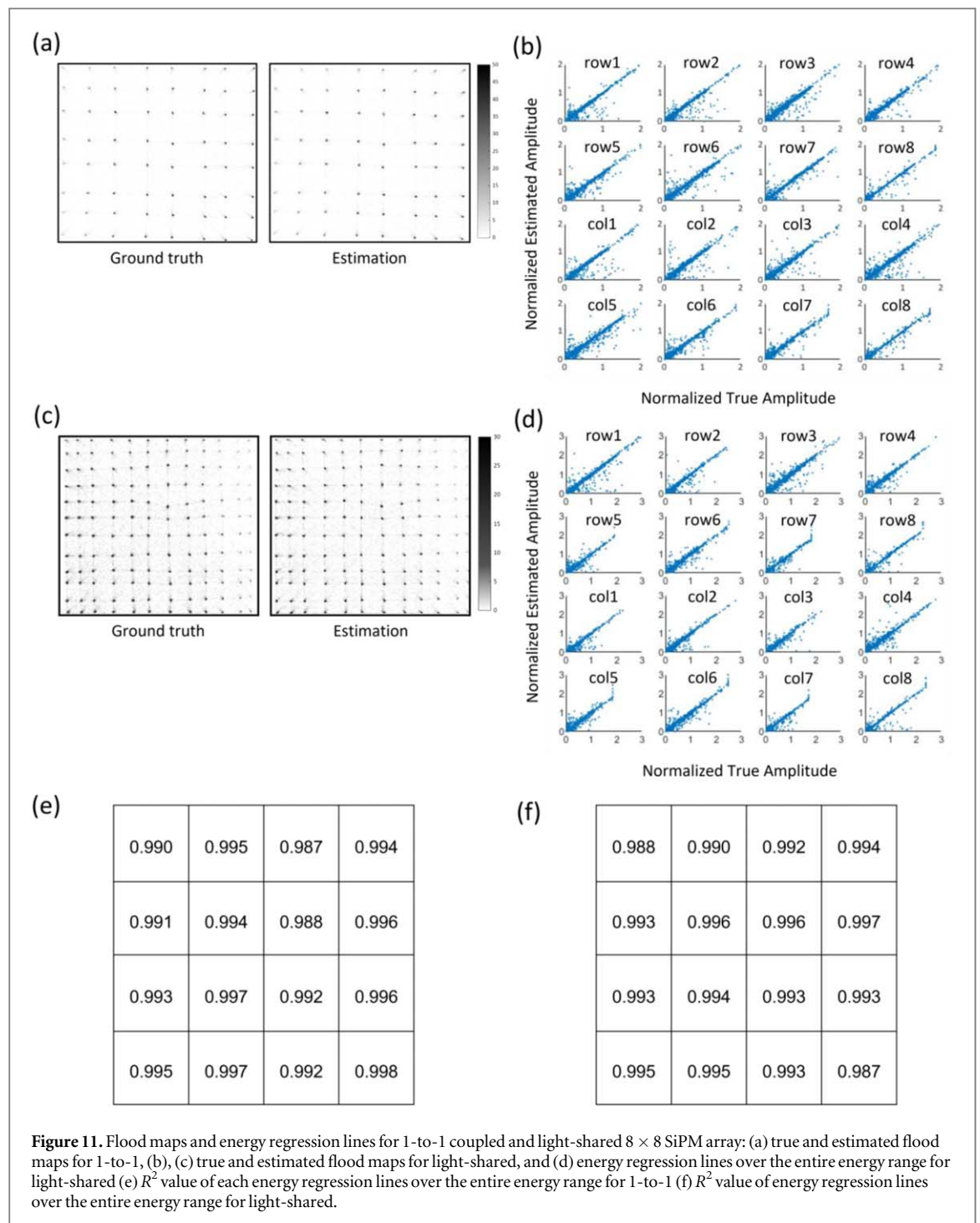
Figure 9 shows the flood maps composed using only the photoelectric events within the energy window that has the same width of energy resolution in each channel (figure 9(a)) and only ICS events with two or more active channels (figure 9(b)). Figure 9(b) was obtained with the energy centroid of multiple positions to visualize the ICS events. Of the total events, the ICS events accounted for 17.01%. Figure 10 shows the energy resolution of the true and estimated energies of 16 channels, yielding all the reasonable values of 8%–11%. Energy resolutions of each channel were calculated using the entire energy spectrum by applying Gaussian fit around 511 KeV photopeak.

### 3.4. Detector-level performance: $8 \times 8$ SiPM

Figure 11 shows the flood maps generated using the center-of-gravity algorithm applied to the true and estimated energies of the row/column summed signals of the 1-to-1 coupled (figures 11(a) and (b)) and light-shared  $8 \times 8$  SiPMs (figures 11(c) and (d)), respectively. Figures 11(b) and (d) show the scatter plots of the true and estimated energies, respectively. Figures 11(e) and (f) show the average  $R^2$  values for all channels at full energy range. For both the 1-to-1 coupled and light-shared detectors, the average  $R^2$  values for all channels were rounded to 0.99 or higher.

### 3.5. Energy estimation of ICS events

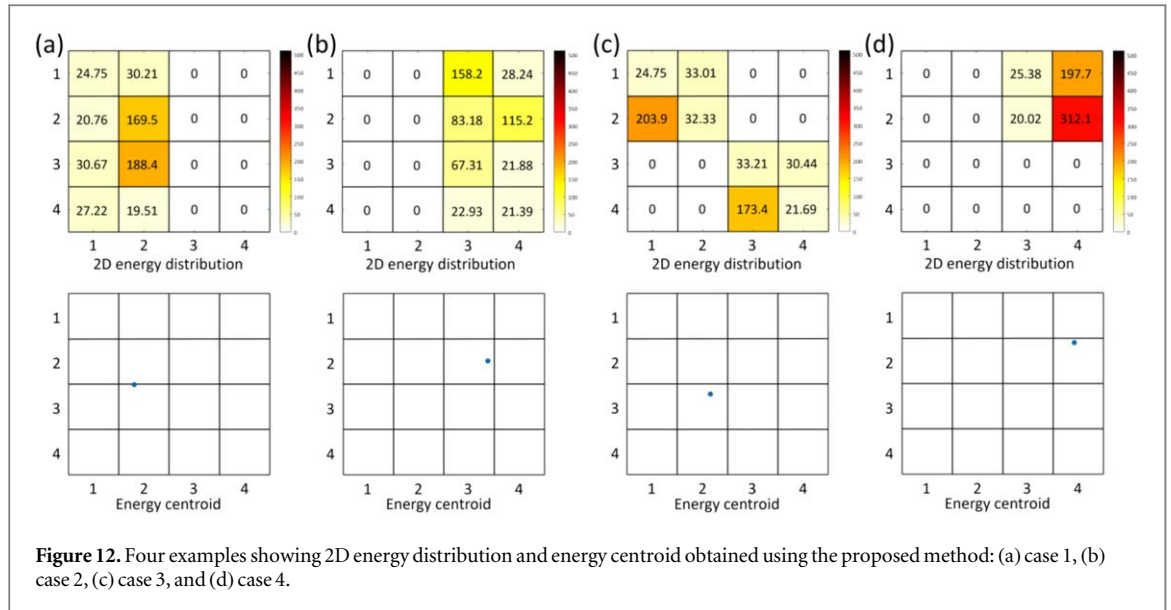
The main advantage of the proposed method is the energy estimation of each SiPM channel from the multiplexed signal, which allows to identify ICS and multiple-events. Figure 12 shows examples of the 2D energy distribution (upper row) and energy centroid (lower row) of the ICS events measured in 1-to-1 coupled  $4 \times 4$  LSO-SiPM detector, which were estimated using the proposed method. The two energy peaks generated by ICS are distinctly evident the estimated 3D energy distribution maps, which were obtained utilizing only four multiplexed readout channels in our proposed method. This is marked improvement compared to the conventional 2D charge division circuits, which only yield energy centroid maps, as depicted in the lower row of figure 12, using the same four readout channels.



## 4. Discussions

### 4.1. Performance difference between the method using the pseudo inverse matrix and the method using the neural network

The performance of the estimation method utilizing the pseudo-inverse matrix has been shown to be unreliable, as evidenced by the results presented in figure 4. This instability can be attributed to several factors. (1) The method assumes a noise-free environment, while the presence of various sources of noise in the circuit can result in substantial errors. (2) The pseudo-inverse matrix approach lacks the constraint that the energy levels of all channels must be positive. As illustrated in figure 4(b), a negative energy estimation is resulted in, which is not physically feasible. (3) The initiation points of the four channels are distinct due to the use of leading-edge discrimination and the difference in the length of circuit pathway. The variance at each starting point can cause significant errors in the estimation. (4) The use of the pseudo-inverse matrix for calculation yields a single



estimate of energy, however, repeated iterations are typically required for the convex optimization. All these issues could be solved using a neural network.

#### 4.2. $R^2$ value between high pass filter sets and channels

Channel 1 was mainly different between Sets 1 and 4. Set 4 with the best performance utilized the largest time constant of the high-pass filter for Channel 1. The results of Set 6, which exhibited the lowest  $R^2$  value, are shown in figure 7. When compared to the results of Set 4, presented in figure 6, there was no substantial difference in the results for Channel 4. Nevertheless, the energy histogram produced using the events of Channel 1 failed to display any notable energy peaks. For each high pass filter sets, Ch1–Ch3 have bigger discrepancy between estimation and truth. The reason why Ch1–Ch3 have bigger discrepancy is that Ch1–Ch3 have a higher cut-off frequency. Therefore, the signal amplitude is smaller for the same gamma ray energy. This effect becomes more pronounced as the channel number increases, with Ch1 having the smallest amplitude and Ch3 the largest. Smaller signal amplitude can lead to lower estimation accuracy. Therefore, Ch1 shows the lowest  $R^2$  value, and more data are observed in small energy region.

#### 4.3. The difference between the energy resolution measured with the ground truth and the estimated energy

The proposed method resulted in successful energy estimation. The discrepancy between ground truth and estimated energy is only approximately 1%. The difference in energy resolution values can be inferred from the difference between the variances in the  $x$ - and  $y$ -directions at the 511 keV peak of the scatter plot. When the variance in the  $x$ -direction exceeds that in the  $y$ -direction, the energy resolution of the estimation using proposed method is larger compared to that of the ground truth, and vice versa. However, this discrepancy would not have a significant impact on the overall image quality.

#### 4.4. Expected impact of the method on image quality improvement

We successfully identified the ICS event by accurately selecting the interacted crystal elements and estimating respective energy depositions of the incident 511 keV gamma-rays. Practical charge division method is intrinsically incapable of ICS identification because it assigns a single crystal closest to the energy centroid of gamma-ray interactions (figure 12). In large portion of ICS events, crystals are differently assigned from the true first interacted one, which induces ICS blurring (Zhang *et al* 2019, Lee and Lee 2021). ICS can occur between crystals that are not adjacent to each other (case 3). As shown in figure 9(b), diagonal lines appear even between the non-neighboring crystals, indicating an ICS event between them. This situation poses a challenge for estimating the first interaction position accurately, using the conventional charge division method. The margin of error can be significantly larger, potentially leading to incorrect estimation of the position in an entirely unrelated crystal.

Such ICS identification would serve as the first step for ICS recovery which is selecting the earliest interacted crystal. Given the position and energy information of the gamma-ray interactions, we can recover ICS events by applying simple energy comparison (Comanor *et al* 1996, Shao *et al* 1996, Surti and Karp 2018) or utilizing complicated Compton scattering physics (Rafecas *et al* 2003, Pratz and Levin 2009, Abbaszadeh *et al* 2018).

Moreover, identified information can be utilized as input of machine learning methods dedicated to ICS recovery (Michaud *et al* 2014, Lee and Lee 2021). Considering that preciseness of energy information is critical for ICS recovery algorithms, good energy resolution of the proposed method is beneficial to achieve high accuracy (figures 6 and 10).

Effect of ICS on PET image quality has been studied by several groups (Ritzer *et al* 2017, Teimoorisichani and Goertzen 2019). Accurately determining the true LORs can alleviate spatial blurring, eventually improving spatial resolution and lesion detectability of PET images (Surti and Karp 2018, Zhang *et al* 2019, Lee *et al* 2020). When combined with accurate ICS recovery algorithms, the proposed method is expected to improve image quality of various PET systems with a relatively small number of read out channels.

#### 4.5. Future work

Because the system level cannot afford a 1 GHz sampling rate, as future work, we plan to test various sampling rates. Higher multiplexing ratios will also be evaluated. To mitigate the need for a dedicated training set, we plan to implement unsupervised transfer learning. Additionally, the feasibility of utilizing the proposed method for efficient ICS recovery needs to be further confirmed.

## 5. Conclusion

In this study, a novel multiplexing method based on the use of high-pass filters and a neural network is proposed for SiPM readouts with the capability of pulse-shape restoration. The energy of signals from 16 channels was effectively restored with  $R^2$  value of 0.99, utilizing only four readouts. The proposed method, in conjunction with the row-and-column sum multiplexing method, achieved a multiplexing ratio to 16:1 in an  $8 \times 8$  SiPM. Furthermore, the proposed approach accurately estimated the 2D energy deposit distribution in the LSO crystal array, enabling the identification of ICS events. In conclusion, the proposed method has the potential to efficiently recover ICS events by reducing the number of required signal readout channels in SiPM arrays.

## Acknowledgments

This work was supported by the Korea Medical Device Development Fund grant funded by the Korea government (the Ministry of Science and ICT, the Ministry of Trade, Industry and Energy, the Ministry of Health & Welfare, the Ministry of Food and Drug Safety) (Project Number: 1711137868, RS-2020-KD000006 and 1711137953, RS-2020-KD000028).

## Data availability statement

The data cannot be made publicly available upon publication because no suitable repository exists for hosting data in this field of study. The data that support the findings of this study are available upon reasonable request from the authors.

## ORCID iDs

Jae Sung Lee  <https://orcid.org/0000-0001-7623-053X>

## References

- Abbaszadeh S, Chinn G and Levin C S 2018 Positioning true coincidences that undergo inter- and intra-crystal scatter for a sub-mm resolution cadmium zinc telluride-based PET system *Phys. Med. Biol.* **63** 025012
- Comanor K A, Virador P R G and Moses W W 1996 Algorithms to identify detector Compton scatter in PET modules *IEEE Trans. Nucl. Sci.* **43** 2213–8
- Downie E, Yang X and Peng H 2013 Investigation of analog charge multiplexing schemes for SiPM based PET block detectors *Phys. Med. Biol.* **58** 3943–64
- Goertzen A L *et al* 2013 Design and performance of a resistor multiplexing readout circuit for a SiPM detector *IEEE Trans. Nucl. Sci.* **60** 1541–9
- Kim D *et al* 2022 Dynamic imaging comparison of 18F-FDG tracers with Compton imaging and PET coincidence imaging *J. Instrum.* **17** C07018
- Ko G B *et al* 2013 Development of a front-end analog circuit for multi-channel SiPM readout and performance verification for various PET detector designs *Nucl. Instrum. Methods Phys. Res. A* **703** 38–44
- Ko G B *et al* 2016 Evaluation of a silicon photomultiplier PET insert for simultaneous PET and MR imaging *Med. Phys.* **43** 72–83
- Kwon S I and Lee J S 2014 Signal encoding method for a time-of-flight PET detector using a silicon photomultiplier array *Nucl. Instrum. Methods Phys. Res. A* **761** 39–45

- Lee J P, Ito M and Lee J S 2011 Evaluation of a fast photomultiplier tube for time-of-flight PET *Biomed. Eng. Lett.* **1** 174–9
- Lee M S, Kang S K and Lee J S 2018 Novel inter-crystal scattering event identification method for PET detectors *Phys. Med. Biol.* **63** 115015
- Lee S, Kim K Y, Lee M S and Lee J S 2020 Recovery of inter-detector and inter-crystal scattering in brain PET based on LSO and GAGG crystals *Phys. Med. Biol.* **65** 195005
- Lee S and Lee J S 2021 Inter-crystal scattering recovery of light-sharing PET detectors using convolutional neural networks *Phys. Med. Biol.* **66** 185004
- Michaud J et al 2014 Sensitivity increase through a neural network method for LOR recovery of ICS triple coincidences in high-resolution pixelated-detectors PET scanners *IEEE Trans. Nucl. Sci.* **62** 82–94
- Olcott P D et al 2013 Cross-strip multiplexed electro-optical coupled scintillation detector for integrated PET/MRI *IEEE Trans. Nucl. Sci.* **60** 3198–204
- Park H, Ko G B and Lee J S 2017 Hybrid charge division multiplexing method for silicon photomultiplier-based PET detectors *Phys. Med. Biol.* **62** 4390–405
- Park H and Lee J S 2020 SiPM signal readout for inter-crystal scatter event identification in PET detectors *Phys. Med. Biol.* **65** 205010
- Park H, Yi M and Lee J S 2022 Silicon photomultiplier signal readout and multiplexing techniques for positron emission tomography: a review *Biomed. Eng. Lett.* **12** 263–83
- Popov V, Majewski S and Welch B L 2006 A novel readout concept for multianode photomultiplier tubes with pad matrix anode layout *Nuclear Nucl. Instrum. Methods Phys. Res. A* **567** 319–22
- Pratz G and Levin C S 2009 Bayesian reconstruction of photon interaction sequences for high-resolution PET detectors *Phys. Med. Biol.* **54** 5073–94
- Rafecas M et al 2003 Inter-crystal scatter in a dual layer, high resolution LSO-APD positron emission tomograph *Phys. Med. Biol.* **48** 821–48
- Ritzer C, Hallen P, Schug D and Schulz V 2017 Intercrystal scatter rejection for pixelated PET detectors *IEEE Trans. Radiat. Plasma Med. Sci.* **1** 191–200
- Shao Y et al 1996 A study of inter-crystal scatter in small scintillator arrays designed for high resolution PET imaging *IEEE Trans. Nucl. Sci.* **43** 1938–44
- Sharma S et al 2020 Estimating relationship between the time over threshold and energy loss by photons in plastic scintillators used in the J-PET scanner *EJNMMI Phys.* **7** 1–15
- Shimazoe K et al 2020 Development of simultaneous PET and Compton imaging using GAGG-SiPM based pixel detectors *Nucl. Instrum. Methods Phys. Res. A* **954** 161499
- Stolin A V et al 2014 Evaluation of imaging modules based on SensL array SB-8 for nuclear medicine applications *IEEE Trans. Nucl. Sci.* **61** 2433–8
- Surti S and Karp J S 2018 Impact of event positioning algorithm on performance of a whole-body PET scanner using one-to-one coupled detectors *Phys. Med. Biol.* **63** 055008
- Teimoorisichani M and Goertzen A L 2019 A study of inter-crystal scatter in dual-layer offset scintillator arrays for brain-dedicated PET scanners *Phys. Med. Biol.* **64** 115007
- Uenomachi M et al 2022 Development of Compton-PET hybrid imaging system with CeBr3-SiPM arrays *J. Instrum.* **17** C10002
- Won J Y, Ko G B and Lee J S 2016 Delay grid multiplexing: simple time-based multiplexing and readout method for silicon photomultipliers *Phys. Med. Biol.* **61** 7113–35
- Yamamoto S, Watabe H and Hatazawa J 2011 Performance comparison of Si-PM-based block detectors with different pixel sizes for an ultrahigh-resolution small-animal PET system *Phys. Med. Biol.* **56** N227–36
- Zhang C et al 2019 The effects of inter-crystal scattering events on the performance of PET detectors *Phys. Med. Biol.* **64** 205004